Electronic Supplementary Information

An Ether Bridge between Cations to Extend the Applicability of Ionic Liquid in Electric Double Layer Capacitors

Hsin-Chieh Huang,[a] Yung-Che Yang,[b] Jui-Cheng Chang,[c] Ching-Wen Su,[a] Pei-Yi Chang,[a] I-Wen Sun,[b] Chien-Te Hsieh,[d] Yuh-Lang Lee,[a] and Hsisheng Teng[a,*]

[a]Department of Chemical Engineering and Research Center for Energy Technology and Strategy, National Cheng Kung University, Tainan 70101, Taiwan

[b]Department of Chemistry, National Cheng Kung University, Tainan 70101, Taiwan

[c]Instrument Center, National Cheng Kung University, Tainan 70101, Taiwan

[d]Department of Chemical Engineering and Materials Science, Yuan Ze Fuel Cell Center, Yuan Ze University, Taoyuan 32023, Taiwan

*To whom correspondenec should be addressed. E-mail: hteng@mail.ncku.edu.tw, Tel: 886-6-2385371, Fax: 886-6-2344496

Electronic supplementary information for:

1. ^{1}H NMR and ^{13}C NMR spectra of $[C_6O_2(MIm)_2]$-$TFSI_2$ (Fig. S1)

2. The chemical structure of $[C_8(MIm)_2]$-$TFSI_2$ (Scheme S1)

3. FTIR spectra of the ILs (Fig. S2)

4. Raman spectra of the ILs (Fig. S3)

5. AC impedance Nyquist plots of the ILs for conductivity measurements (Fig. S4)

6. Linear scan voltammograms for determining the usable voltage ranges of the

ILs (Fig. S5)

7. Pore size distribution of the aMP carbon (Table S1)

8. Cyclic voltammograms of the EMIm-TFSI and EM-di5 EDLCs measured at 60 ºC (Fig. S6)

9. Capacitance values of the EMIm-TFSI and EM-di5 EDLCs measured at 60 ºC (Fig. S7)

1. ^{1}H NMR and ^{13}C NMR spectra of $[C_6O_2(MIm)_2]$-$TFSI_2$

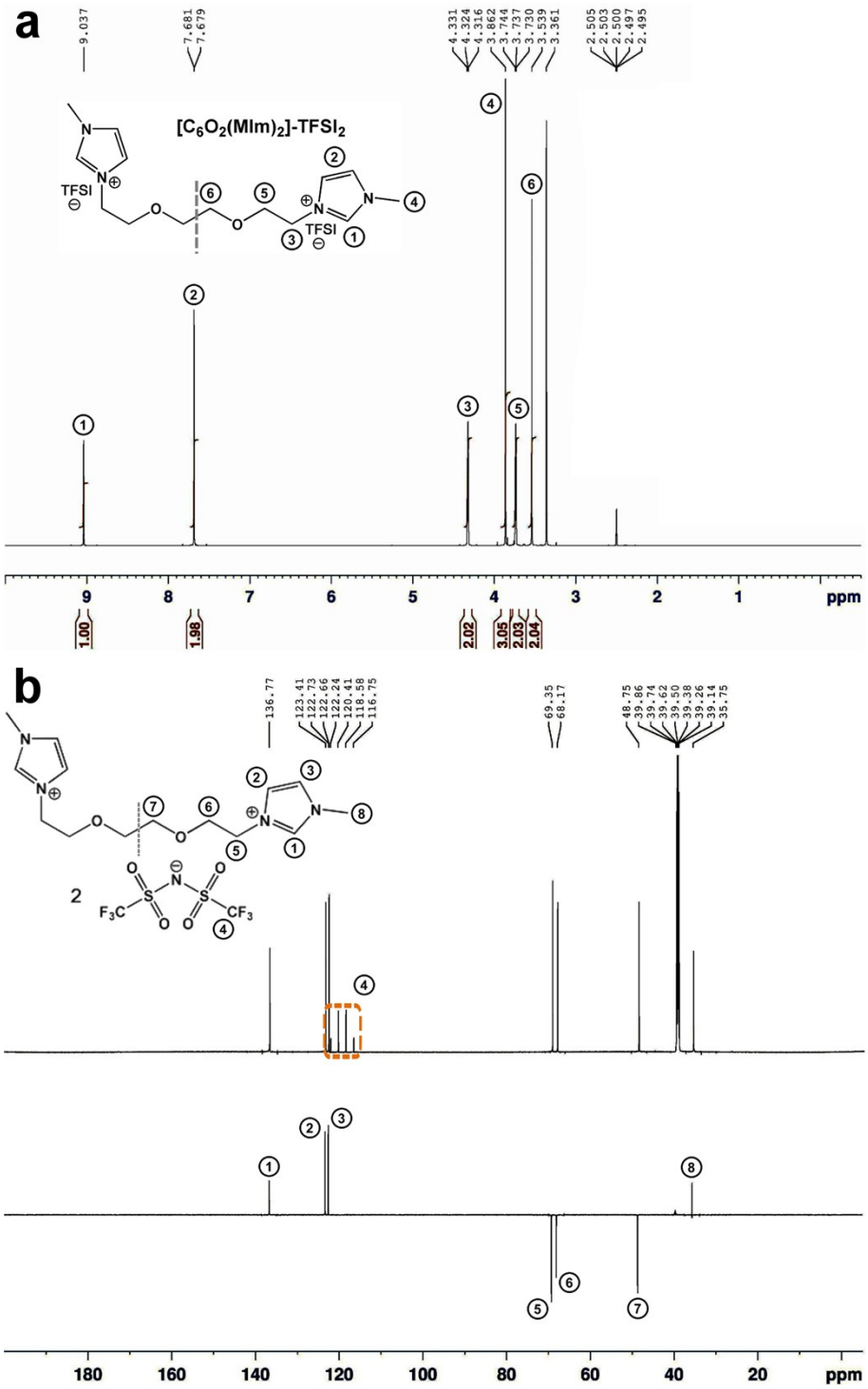

Fig. S1. The (a) ^{1}H NMR and (b) ^{13}C NMR spectra of $[C_6O_2(MIm)_2]$-$TFSI_2$ reveal the distinct types of hydrogen and carbon atoms in cation and anion. The numbers beside the NMR peaks correspond to the distinct hydrogen or carbon atoms in molecular structure.

2. The chemical structure of $[C_8(MIm)_2]$-$TFSI_2$

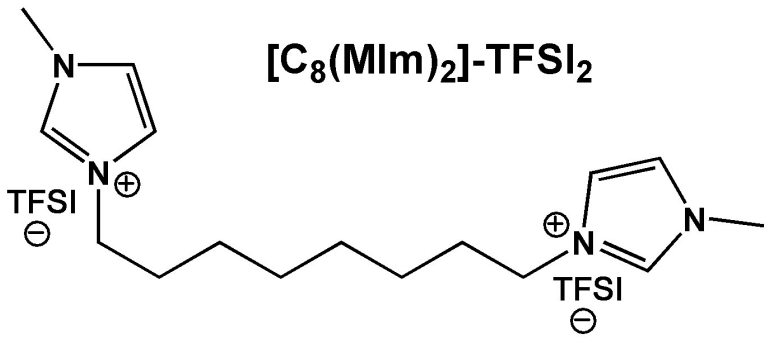

Scheme S1. Schematic illustration of the chemical structure of the $[C_8(MIm)_2]$-$TFSI_2$ DIL containing an ethylene-chain-bridge.

3. FTIR spectra of the ILs

Fig. S2a shows the full-range Fourier transform infrared (FTIR) spectra associated with EM-di0, EM-di5, and $[C_6O_2(MIm)_2]$-$TFSI_2$. In the region between 650 and 900 cm^{-1} (Fig. S2b), five strong bands were observed, and they were assigned to a S–N–S bending (652 cm^{-1}), CF_3 symmetric bending (741 cm^{-1}), ring HCCH asymmetric bending (763 cm^{-1}), C–S stretching (791 cm^{-1}), and NC(H)N bending/CCH bending (837 cm^{-1}).[35–37] Other strong bands are shown in Fig. S2c, and they were assigned to a S–N–S asymmetric stretching, C–C stretching, NCH_3 twisting (1053 cm^{-1}), SO_2 symmetric stretching (1134 cm^{-1}) overlapping an asymmetric C–O–C stretching in an ether-bridged linker of $[C_6O_2(MIm)_2]$-$TFSI_2$ (1120 cm^{-1}),[33] and a $CH_2(N)/CH_3(N)$ C–N stretching (1169 cm^{-1}). Between 1180 and 1350 cm^{-1}, the anions dominated, particularly in terms of CF_3 asymmetric stretching (1180 and 1198 cm^{-1}), CF_3 symmetric stretching (1227 cm^{-1}), and two SO_2 asymmetric stretching modes (1331 and 1350 cm^{-1}).[35–37] We noted that a ring in-plane $CH_2(N)/CH_3(N)$ symmetric/asymmetric stretching mode involved wavenumber shifts (1575 cm^{-1} for EMIM-TFSI, 1574 cm^{-1} for EM-di5, and 1577 cm^{-1} for $[C_6O_2(MIm)_2]$-$TFSI_2$), indicating that the vibration behavior of $CH_2(N)$ and $CH_3(N)$ in the imidazolium cations demonstrated the highest freedom in the movements of EM-di5. However, the linker exerted a greater constraint on $[C_6O_2(MIm)_2]$-$TFSI_2$ than on the MIL that was translated by the wavenumber shift to a higher value.[38,39] Fig. S2d (2800 to 3300 cm^{-1}) shows the C–H stretching band where $[C_6O_2(MIm)_2]$-$TFSI_2$ has a stronger intensity than that of EM-di0 because of the linker.[36]

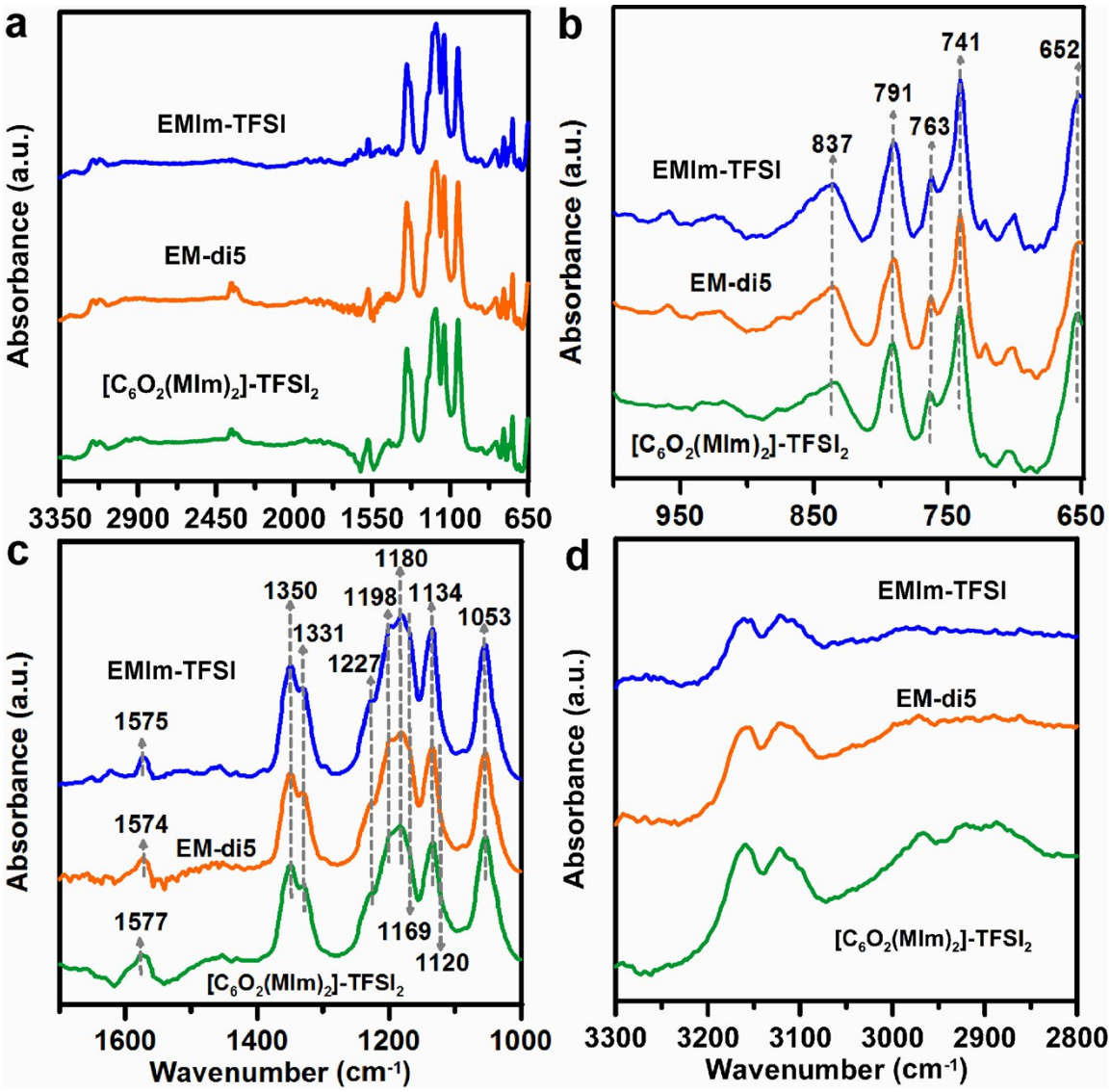

Fig. S2. The FTIR spectra of EMIm-TFSI, EM-di5, and $[C_6O_2(MIm)_2]$-$TFSI_2$ in (a) the full spectral range 3350–650 cm^{-1}, (b) the spectral range 1000–650 cm^{-1}, (c) the spectral range 1700–1000 cm^{-1}, and (d) the spectral range 3300–2800 cm^{-1}.

4. Raman spectra of the ILs

Fig. S3a shows the full-range Raman spectra of EMIm-TFSI, EM-di5, and $[C_6O_2(MIm)_2]$-$TFSI_2$. The strongest signal was at 742 cm^{-1}, and it was assigned to the CF_3 symmetric stretching of the TFSI anion. Fig. S3b presents a CF_3 symmetric bending (280 cm^{-1}) and S–C stretching (314, 328, and 340 cm^{-1}). In addition, a signal of $CH_2(N)/CH_3(N)$ C–H bending was located as $[C_6O_2(MIm)_2]$-$TFSI_2$ (407 cm^{-1}) > EMIm-TFSI (403 cm^{-1}) > EM-di5 (401 cm^{-1}), signifying that the interionic interaction between the imidazolium cations and the TFSI anions of $[C_6O_2(MIm)_2]$-$TFSI_2$ was the strongest, whereas that of EM-di5 was the weakest.[38,39] The linker limited $[C_6O_2(MIm)_2]$-$TFSI_2$ mobility so that $[C_6O_2(MIm)_2]$-$TFSI_2$ had a high viscosity and high interionic and intermolecular interaction. By contrast, when a small amount of $[C_6O_2(MIm)_2]$-$TFSI_2$ was added to EMIm-TFSI, the interionic interaction between the cations and anions decreased. The same phenomenon was observed at a $CH_2(N)/CH_3(N)$ C–N stretching mode: $[C_6O_2(MIm)_2]$-$TFSI_2$ (601 cm^{-1}) > EM-di0 (599 cm^{-1}) > EM-di5 (598 cm^{-1}), as shown in Fig. S3b, and $[C_6O_2(MIm)_2]$-$TFSI_2$ (1575 cm^{-1}) > EM-di0 (1573 cm^{-1}) > EM-di5 (1570 cm^{-1}), as shown in Fig. S3c; we also note another O=S=O asymmetric stretching mode: $[C_6O_2(MIm)_2]$-$TFSI_2$ (1341 cm^{-1}) > EM-di0 (1337 cm^{-1}) > EM-di5 (1336 cm^{-1}).[38,39] Moreover, other strong Raman bands (Fig. S3c) were assigned to a C–F symmetric stretching (1025 and 1244 cm^{-1}), C–C stretching (only for $[C_6O_2(MIm)_2]$-$TFSI_2$ at 1038 cm^{-1}), SO_2 symmetric stretching (1138 cm^{-1}), and $CH_2(N)/CH_3(N)$ C–N stretching (1390, 1422, and 1456 cm^{-1}). Fig. S3d shows the C–H stretching region (2900 to 3000 cm^{-1}) assigned to the vibration of the ethyl chain on the imidazolium cations in the same FTIR spectral zone.[36]

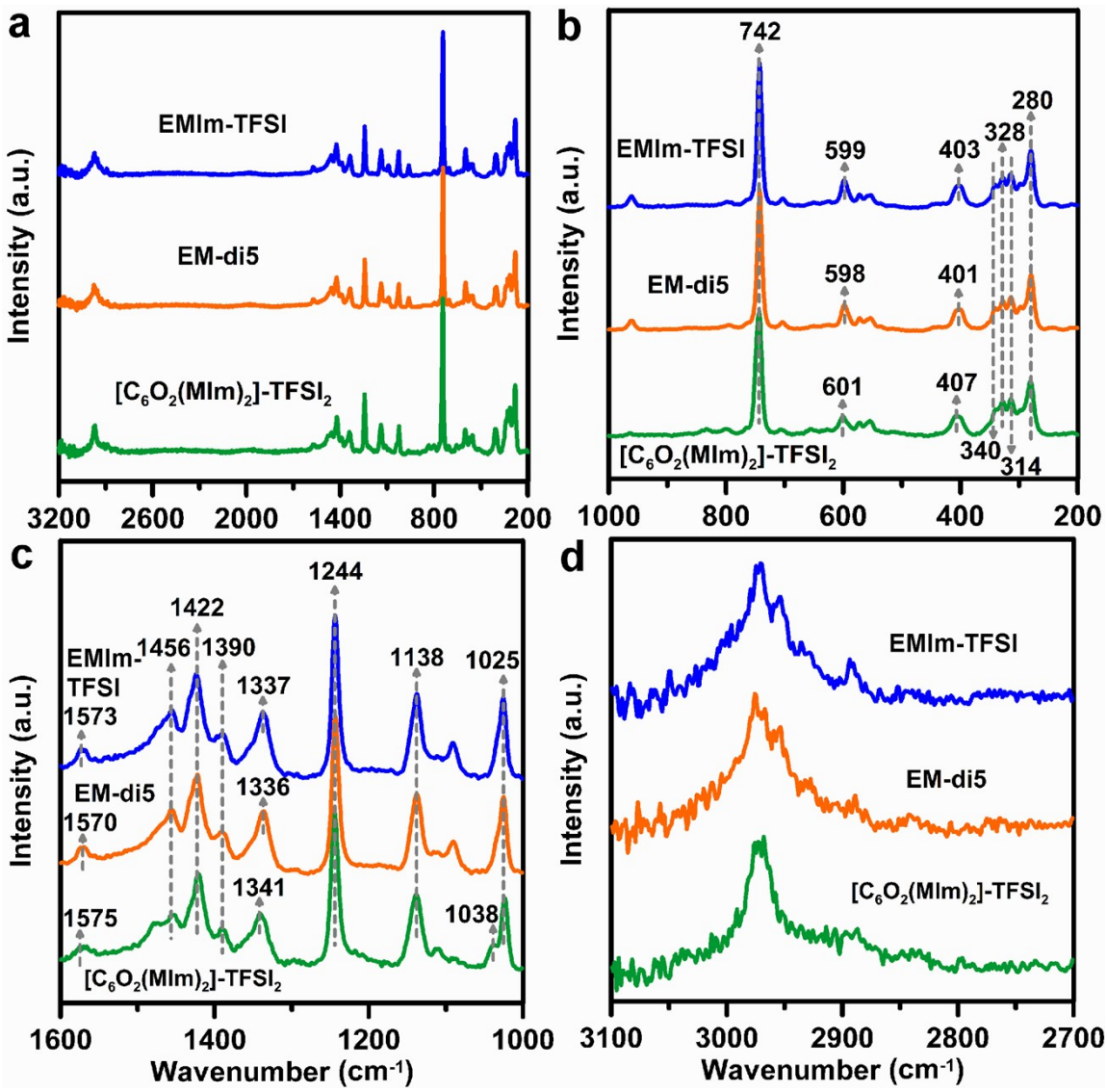

Fig. S3. The Raman spectra of EMIm-TFSI, EM-di5, and $[C_6O_2(MIm)_2]$-$TFSI_2$ in (a) the full spectral range 3200–200 cm^{-1}, (b) the spectral range 1000–200 cm^{-1}, (c) the spectral range 1600–1000 cm^{-1}, and (d) the spectral range 3100–2700 cm^{-1}.

5. AC impedance Nyquist plots of the ILs for conductivity measurements

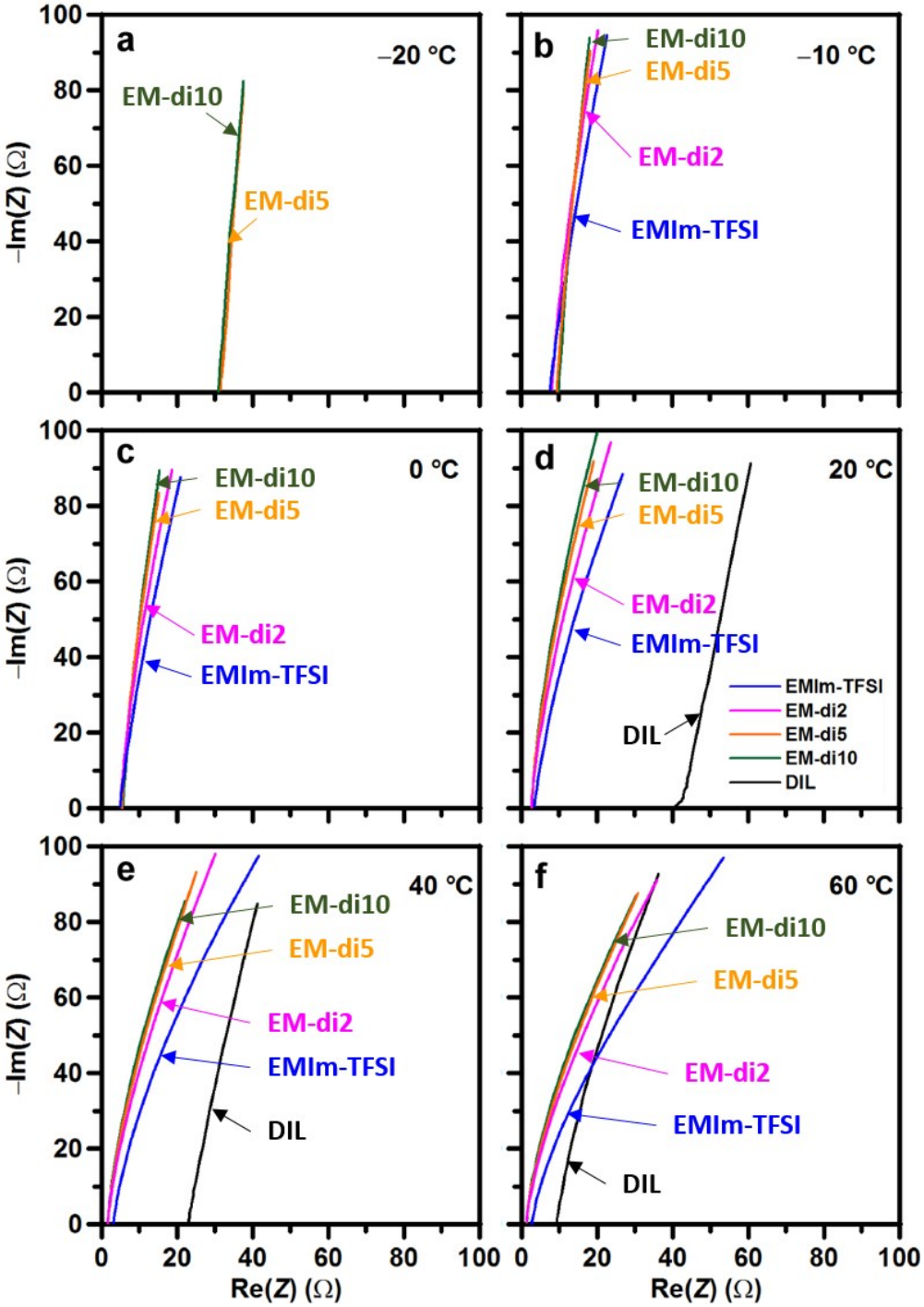

Fig. S4. Nyquist impedance plots of the IL electrolytes measured at temperatures of –20 to 60 °C with an AC frequency range of 0.1 Hz to 1 MHz at 0 V. In the measurement, the electrolytes were soaked with a cellulose membrane that was then placed between two stainless steel foils of 1 cm^2. The thickness of the cellulose membrane was 30 μm.

6. Linear scan voltammograms for determining the usable voltage ranges of the ILs

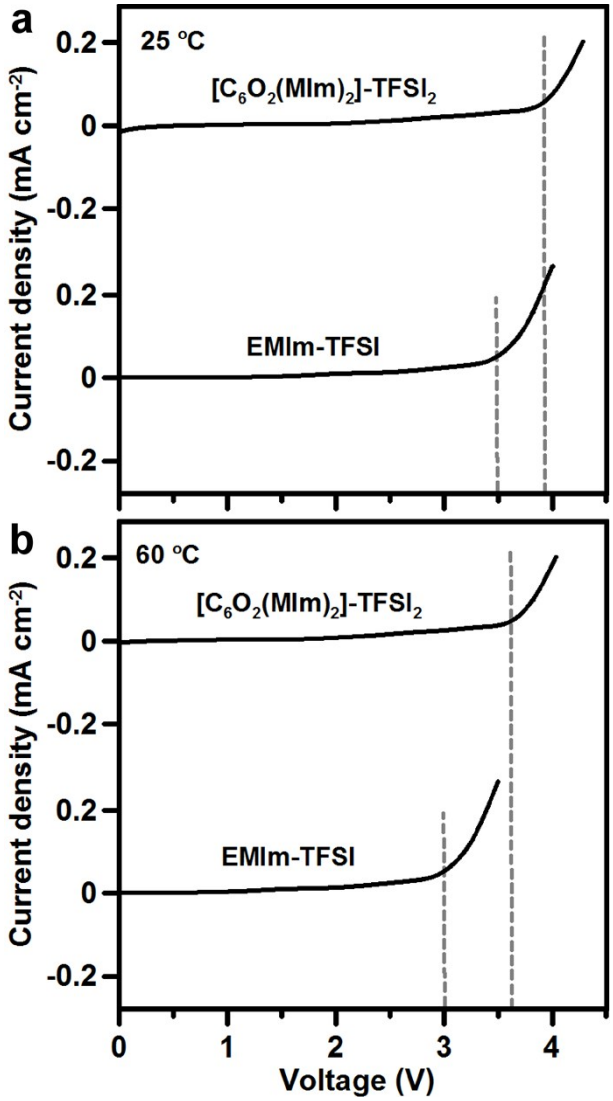

Fig. S5. The linear scan voltammograms of the EMIm-TFSI and $[C_6O_2(MIm)_2]$-$TFSI_2$ cells used in the conductivity analysis (Fig. S4). The voltammograms were obtained at 25 and 60 °C by scanning from 0 V at a scan rate of 5 mV s^{-1}.

7. Pore size distribution of the aMP carbon

Table S1. Pore structure of the aMP carbon. S_{BET} represents the surface area determined using the Brunauer–Emmett–Teller method, S_t and V_t the surface area and pore volume determined using the non-local density functional theory, and S_{mi} the micropore (0.58–2 nm) surface area determined using the non-local density functional theory. V_t is contributed by micropores (< 2 nm) and mesopores (2–100 nm), with the contribution percentages shown in the "Pore size distribution" column.

Carbon	S_{BET} ($m^2\ g^{-1}$)	S_t ($m^2\ g^{-1}$)	S_{mi} ($m^2\ g^{-1}$)	V_t ($cm^3\ g^{-1}$)	Pore size distribution	
					Micro (%)	Meso (%)
aMP	2700	1767	1400	1.46	63	37

8. Cyclic voltammograms of the EMIm-TFSI and EM-di5 EDLCs measured at 60 °C

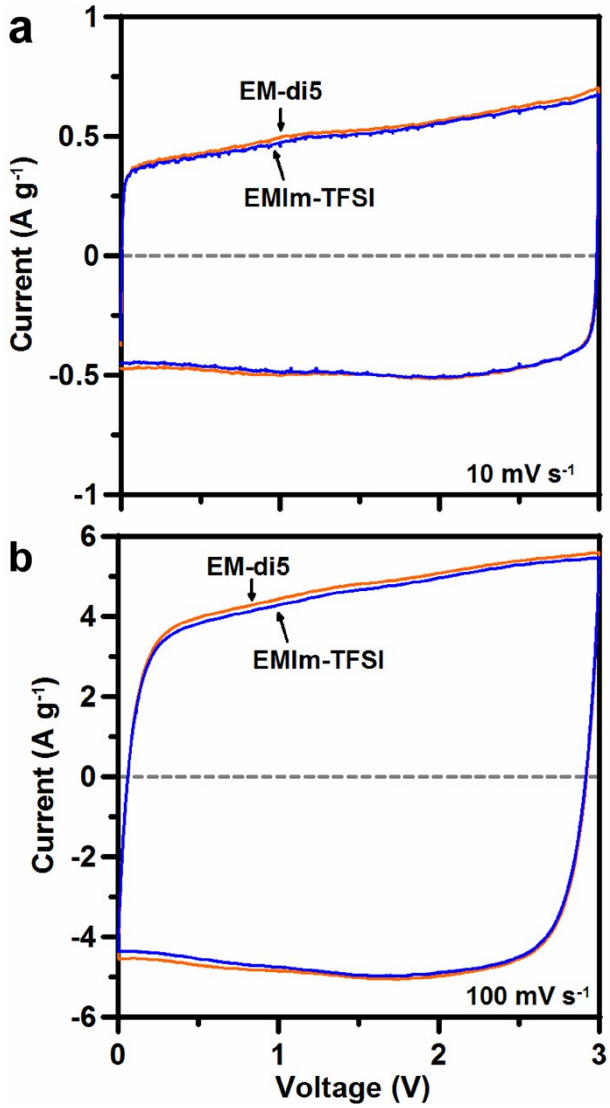

Fig. S6. Cyclic voltammograms of the EMIm-TFSI and EM-di5 EDLCs measured at 60 °C with scan rates of: (a) 10 mV s^{-1}; (b) 100 mV s^{-1}.

9. Capacitance values of the EMIm-TFSI and EM-di5 EDLCs measured at 60 °C

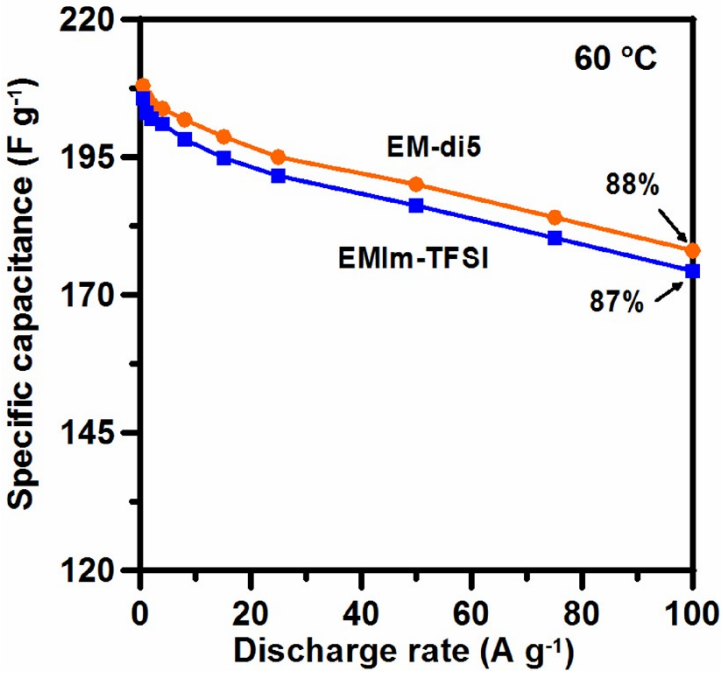

Fig. S7. The variation of the capacitance at 60 ºC with discharge rate for the EMIm-TFSI and EM-di5 EDLCs.